Journal of the Mechanics and Physics of Solids 70 (2014) 349–361

Contents lists available at ScienceDirect

Journal of the Mechanics and Physics of Solids

journal homepage: www.elsevier.com/locate/jmps

# A chemo-mechanical model of lithiation in silicon

Hui Yang [a], Feifei Fan [b], Wentao Liang [a], Xu Guo [c], Ting Zhu [b], Sulin Zhang [a,*]

[a] Department of Engineering Science and Mechanics, Pennsylvania State University, University Park, PA 16802, United States
[b] Woodruff School of Mechanical Engineering, Georgia Institute of Technology, Atlanta, GA 30332, United States
[c] State Key Laboratory of Structural Analysis for Industrial Equipment, Department of Engineering Mechanics, Dalian University of Technology, Dalian 116023, PR China

ARTICLE INFO

*Article history:*
Received 28 June 2013
Received in revised form
9 June 2014
Accepted 15 June 2014
Available online 21 June 2014

*Keywords:*
Lithium-ion battery
Diffusion
Large-strain plasticity
Anisotropic swelling
Fracture

ABSTRACT

We present a chemo-mechanical model to investigate the lithiation-induced phase transformation, morphological evolution, stress generation and fracture in crystalline silicon nanowires (*c*-SiNWs). The model couples lithium (Li) diffusion with elasto-plastic deformation in a three-dimensional (3D) setting. Several key features observed from recent transmission electron microscopy (TEM) studies are incorporated into the model, including the sharp interface between the lithiated amorphous shell and unlithiated crystalline core, crystallographic orientation dependent Li–Si reaction rate, and large-strain plasticity. Our simulation results demonstrate that the model faithfully predicts the anisotropic swelling of lithiated SiNWs observed from previous experimental studies. Stress analysis from the finite-deformation model reveals that the SiNWs are prone to surface fracture at the angular sites where two adjacent {110} facets intersect, consistent with previous experimental observations. The mechanistic understanding of the morphological evolution and stress generation sheds light on the design of failure-resistant nanostructured electrodes. Our model offers a framework for the study of the chemo-mechanical degradation in high-capacity electrode materials.



## 1. Introduction

The high-capacity Lithium (Li) ion batteries (LIBs) are critically important for portable electronics, hybrid electric vehicles, and large-scale energy storage (Arico et al., 2005; Service, 2011; Tarascon and Armand, 2001). This has stimulated enormous efforts to the development of new electrode materials that are not only of high energy and high power densities, but also electro-chemo-mechanically reliable (Bindumadhavan et al., 2013; Liang et al., 2013; Liu et al., 2011a, 2012c, 2011d; Marom et al., 2011; Wu et al., 2012; Yao et al., 2011; Zhang, 2011). A number of high-capacity electrode materials have been recently studied, among which silicon stands as the leading candidate with its theoretical capacity one order of magnitude higher than conventional graphite anodes (Chan et al., 2008; Liu et al., 2011b; Marom et al., 2011; Obrovac and Christensen, 2004; Zhang, 2011). However, inherent to the high-capacity electrodes, Li insertion/extraction induces large volumetric change and stress inside the electrodes, causing degradation and cracking (Beaulieu et al., 2001; Cui et al., 2009; Goldman et al., 2011; Magasinski et al., 2010; Scrosati et al., 2011). The issue becomes more significant when an electrode undergoes high-rate charging or discharging, which often induces non-uniform Li distribution in the electrodes. The resulting large incompatible deformation between regions with different Li concentrations tends to initiate fracture in the electrodes.

* Corresponding author.
*E-mail address:* suz10@psu.edu (S. Zhang).

http://dx.doi.org/10.1016/j.jmps.2014.06.004
0022-5096/

Subsequent crack propagation and failure may cause the loss of electrical contact between active materials, current collectors, and electrolytes, leading to fast capacity fading and poor cyclability. Chemo-mechanical degradation is one of the major challenges in the development of next-generation high-performance LIBs.

It has been recognized that nanoscale electrode materials can facilitate strain relaxation, enhance flaw tolerance, shorten Li ion and electron diffusion paths, and increase surface area for Li-electrode reaction (Bruce et al., 2008; Park et al., 2009). Therefore, scaling the size of electrode materials down to the nanometer range represents one of the promising strategies to drastically improve the electrode performance (Chan et al., 2008; Hertzberg et al., 2010; Li et al., 1999; Yamada et al., 2011; Yao et al., 2011; Zhang et al., 2011). Recent experimental studies on the size effect have demonstrated that nanoscale materials indeed exhibit better capacity retention as compared to their bulk counterparts (Lee et al., 2012; Liu et al., 2012d; Ryu et al., 2011). The promise of nanomaterials also motivated the development of new experimental platforms for real-time studies of electrode degradation at the nanoscale. In these works, a nanoscale battery is assembled, where the electrodes are comprised of nanoparticle or nanowire arrays, or even single nanoparticles and nanowires (Lee et al., 2011; Liang et al., 2013; Liu et al., 2012b, 2012c, 2011b, 2011c; McDowell et al., 2013; Sun et al., 2013; Wang et al., 2013). The electrochemical cycling responses of the nano-battery were monitored by an *in-situ* high-resolution transmission electron microscope (HRTEM) (Liu and Huang, 2011; Liu et al., 2011c; McDowell et al., 2013). This experimental setup allows real-time tracking of the tempo-spatial evolution of large deformation, crack nucleation and propagation, and phase transformation during electrochemical cycling, thereby offering a unique platform for the study of degradation mechanisms in electrodes.

Recent scanning electron microscope (SEM) and TEM studies have revealed a range of novel phenomena during lithiation of Si nanowires (SiNWs) and nanoparticles (SiNPs) (Goldman et al., 2011; Lee et al., 2012, 2011; Liu et al., 2012a, 2012b, 2011b, 2011c; McDowell et al., 2013). Upon lithiation, crystalline SiNWs (*c*-SiNWs) not only undergo large volume expansion ($\sim$300%) (Liu et al., 2011b), but also swell in an anisotropic manner (Goldman et al., 2011; Lee et al., 2011; Liu et al., 2011c), with predominant expansion along the $\langle 110\rangle$ direction, but negligibly small expansion along the $\langle 111\rangle$ direction (Liu et al., 2011c). The anisotropic swelling results in a range of unique cross-sectional morphologies in fully lithiated SiNWs, depending on the crystallographic orientations of *c*-SiNWs (Lee et al., 2011; Liu et al., 2011c), as shown in Fig. 1. SEM and TEM studies further show that crack nucleates from the surface of lithiated SiNWs or SiNPs (Lee et al., 2012; Liang et al., 2013; Liu et al., 2011c, 2012d). Subsequent crack extension not only depends on the size of SiNWs and SiNPs, but also occurs along the specific directions dictated by the crystallographic structure of the pristine crystalline Si (*c*-Si) (Lee et al., 2012; Liang et al., 2013; Liu et al., 2012d). More recently, it has been observed that lithiation of SiNWs or SiNPs slows down as lithiation proceeds, indicating that mechanical stress generated in the lithiation process can drastically retard chemical reaction at the reaction front and/or the Li diffusion in the lithiated regions (Liu et al., 2012a; McDowell et al., 2012).

Despite the rapid advance in experimental studies, models that are versatile enough to capture the key experimental phenomena and reveal their mechanistic origins are still lacking. Herein, we aim to develop a chemo-mechanical model for the study of morphological evolution, stress generation, and fracture in lithiated Si. The model couples Li reaction–diffusion with large elasto-plastic deformation in a three-dimensional (3D) setting. In addition, the model incorporates several key physical features observed from TEM studies, and is thus faithful to the underlying chemo-mechanical mechanisms. The modeling framework is generic and thus applicable to study the degradation mechanisms in a variety of high-capacity electrodes.

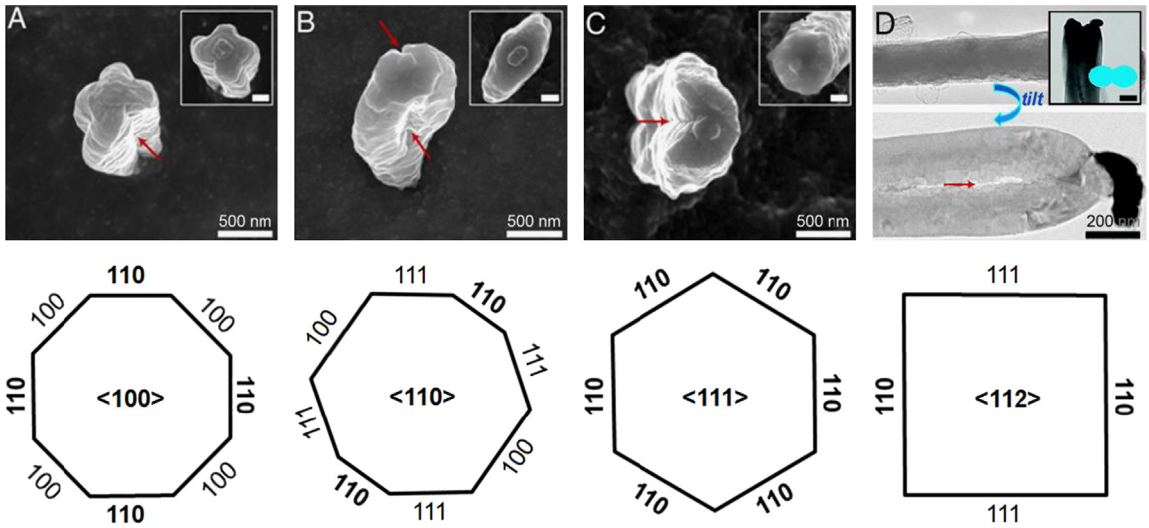


**Fig. 1.** SEM (Lee et al., 2012. Reprinted with permission. Copyright 2012, National Academy of Sciences.) and TEM (Liu et al., 2011c. Reprinted with permission. Copyright 2011, American Chemical Society.) images of anisotropic swelling and fracture in lithiated SiNWs with four different axial orientations: (A) $\langle 100\rangle$, (B) $\langle 110\rangle$, (C) $\langle 111\rangle$, and (D) $\langle 112\rangle$. Top: Cracks oriented along the axes of the SiNWs are indicated by red arrows. Bottom: The corresponding crystallographic orientations of the facets on the sidewalls of each SiNW are shown (Yang et al., 2012. Reprinted with permission. Copyright 2012, American Chemical Society.). The scale bars in the insets are 200 nm. (For interpretation of the references to color in this figure legend, the reader is referred to the web version of this article.)

The rest of the article is organized as follows. Section 2 discusses several key features observed in TEM experiments, which form the physical basis of the chemo-mechanical model. Section 3 formulates the chemo-mechanical model, with special attention paid to the mathematical incorporation of these key physical features. Section 4 implements the model by finite element methods. Section 5 reports major numerical results on the morphological evolution and stress generation of the SiNWs under lithiation. Possible extensions of the model are discussed in Section 6 and conclusions are drawn in Section 7.

## 2. Key physical features in lithiation of crystalline Si

### 2.1. Sharp phase boundary

During electrochemical lithiation, Li reacts with and diffuses within Si. Since the Li mobility on the surface is much larger than in the bulk, Li tends to first cover the surface of SiNWs or SiNPs before radial Li flow starts (Liu et al., 2011c, 2012d; McDowell et al., 2012; Zhang et al., 2010). Recent *in-situ* TEM studies revealed that lithiation of *c*-SiNWs or *c*-SiNPs proceeds through the migration of an atomically sharp reaction front ($\sim$1 nm in width) that separates the lithiated amorphous shell of $Li_xSi$ alloy and the *c*-Si core (Fig. 2) (Chon et al., 2011; Liu et al., 2012b, 2011b, 2011c). The Li concentration within the unlithiated core is apparently low, evidenced by the intact lattice structure with the measured lattice spacing close to that of pristine *c*-Si (Liu et al., 2012b, 2011b, 2011c). The lithiated phase likely consists of amorphous $Li_{3.75}Si$ since its volume expansion is close to that of crystalline $Li_{3.75}Si$ (Liu et al., 2012b, 2011c). The lithiation reaction front is therefore identified as a phase boundary, across which an abrupt change of Li concentration occurs. Namely, the Li-poor and Li-rich phases do not transform continuously into each other with changing composition, and lithiation proceeds by the phase boundary migration. The sharp interface plays a vital role in stress generation and fracture in *c*-Si during lithiation (Liang et al., 2013; McDowell et al., 2012). A mechanistic model thus requires a faithful description of co-evolution of the two phases with a sharp phase boundary.

### 2.2. Time scales of reaction and diffusion

Lithiation of SiNWs involves two processes in series: Li diffusion through the lithiated shell and chemical reaction at the phase boundary. The characteristic time of long-range Li diffusion scales with $t_D \sim L^2/D$ (Bruce et al., 2008), where $L$ and $D$ are the sample size and the Li diffusivity in lithiated amorphous Si, respectively. On the other hand, Li–Si reaction is a short-range process involving the dissociation of the Si–Si bonds and formation of the lithiated amorphous product at the reaction front. The characteristic time scale $t_R$ of Li–Si reaction (i.e., of reaction front migration) is $L/k$, where $k$ is the rate constant of reaction. A critical length scale, $L_{cr} = D/k$, exists. For nanometer-sized samples, $L \ll L_{cr}$. The reaction front under this condition propagates much slower than the Li diffusion behind it, and lithiation is limited by the interfacial reaction. On the contrary, for large specimens, $L \gg L_{cr}$, and lithiation is limited by diffusion. A transition between the two rate-limiting mechanisms exists at an intermediate size of $L$.

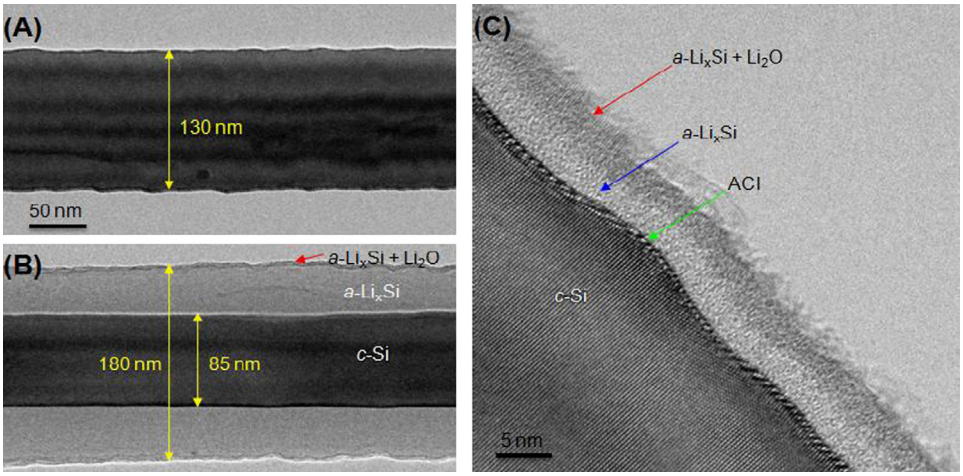


**Fig. 2.** *In-situ* TEM experiment of lithiation of a ⟨112⟩ *c*-SiNW. (A) TEM image of a *c*-SiNW prior to lithiation. (B) Formation of a core–shell structure in a partially lithiated SiNW, where the crystalline core (*c*-Si) is surrounded by the amorphous shell (*a*-$Li_xSi$). A thin layer of $Li_2O$ is formed on the outer surface of the lithiated shell. (C) The amorphous–crystalline interface (ACI), i.e., the phase boundary separating the amorphous lithiated shell and the unlithiated crystalline core, is atomically sharp (~1 nm) (Liu et al., 2012b. Reprinted with permission. Copyright 2012, Macmillan Publishers Limited.).

### 2.3. Lithiation anisotropy

There have been debates regarding the origin of anisotropic swelling of *c*-Si upon lithiation when the experimental observations were first reported. Considering the core–shell structure in a partially lithiated SiNW or SiNP, the elasto-plastic properties and Li diffusivity in the fully lithiated shell are both isotropic because of its amorphous structure. In the pristine crystalline core, the cubic structure of Si crystal renders isotropic Li diffusivity (Newnham, 2005), but anisotropic elastic properties. Owing to the lithiation-induced strain mismatch, the crystalline core undergoes elastic deformation. The anisotropic elastic properties of *c*-Si could lead to stress anisotropy, which could in turn cause anisotropic reaction rate near the reaction front, considering that chemical reaction rate is generally stress-dependent. However, the order of elastic anisotropy (with elastic moduli $Y_{\langle 111\rangle} > Y_{\langle 110\rangle} > Y_{\langle 100\rangle}$) is inconsistent with that of lithiation-induced expansion ($\varepsilon_{\langle 110\rangle} > \varepsilon_{\langle 100\rangle} > \varepsilon_{\langle 111\rangle}$), which excludes the possibility of the dominant role of elastic anisotropy. In addition, the marginal anisotropy in the elastic properties (elastic moduli differ by only $\sim$10% in $\langle 111\rangle$ (189 GPa) and $\langle 110\rangle$ (169 GPa) directions (Wortman and Evans, 1965) unlikely accounts for the considerable anisotropy of expansions in lithiated SiNWs (swelling in $\langle 110\rangle$ is about 9 times that in $\langle 111\rangle$). This leaves only one possible origin of the anisotropic swelling: the crystallographic orientation dependence of the Li–Si reaction rate at the sharp phase boundary (Yang et al., 2012; Zhao et al., 2012).

The orientation dependence of reaction rate was recently verified by *in-situ* HRTEM studies (Liu et al., 2012b). It has been observed that lithiation of *c*-Si proceeds by the migration of an amorphous-crystalline interface (ACI) (Liu et al., 2012a, 2012b, 2011c, 2012d). The interface migration occurs through a ledge mechanism, involving lateral movement of ledges on the close-packed {111} atomic planes (Liu et al., 2012b). These ledges are usually inclined to the ACI (except for the {111} interface), leading to the orientation dependence of interfacial migration velocity. The *in-situ* HRTEM shows that the phase boundary migrates much faster along $\langle 110\rangle$ directions (several nanometers per minute) than other directions, while the interfacial migration velocity is at least one order of magnitude lower along $\langle 111\rangle$ directions (Liu et al., 2012b).

The orientation dependence of lithiation rate at the reaction front affects not only the morphology of the fully lithiated Si structures, but also the subsequent fracture (Lee et al., 2012; Liang et al., 2013). At the fastest-moving {110} interface, the large volumetric expansion occurs due to an abrupt increase of Li concentration across the interface. Such expansion tends to push the lithiated product behind the moving interface outward (Huang et al., 2013; Liang et al., 2013; McDowell et al., 2012; Yang et al., 2012). As a consequence of the outward pushing normal to {110} interfaces, large incompatible strains are generated at the intersections of adjacent {110} facets (particularly near the outer surface), leading to crack nucleation at well-defined angular sites (Liang et al., 2013).

### 2.4. Lithiation-induced large deformation

Lithiation of *c*-Si can characteristically results in amorphous alloys and large deformation. It is now well-accepted that lithiated Si undergoes material remodeling through plastic flow (Sethuraman et al., 2010a), generating unique deformation morphologies (Goldman et al., 2011; Lee et al., 2011; Liu et al., 2011c). The lithiation-induced deformation is expected to be large and well beyond the applicable region of small-strain theory. Indeed, as demonstrated in our previous simulations, the small-strain theory may be still suited to approximate the morphological evolution, but inadequate to accurately predict stress distribution in the SiNWs under lithiation (Yang et al., 2012). It is important to note that the small-strain theory predicts a nearly uniform principal stress within the lithiated shell. This would imply that crack nucleation might be equally possible at any location near the surface of the lithiated SiNWs, in contradiction with the well-defined surface fracture sites observed in recent SEM and TEM studies (Lee et al., 2012; Liang et al., 2013; Liu et al., 2011c). Such inadequacy suggests that the finite-strain plasticity theory should be invoked to accurately compute stress generation during lithiation, since it is essential to use the appropriate strain and stress measures and associated constitutive relations that distinguish the reference and deformed configurations (ABAQUS, 2010).

## 3. A chemo-mechanical model

### 3.1. Evolving two-phase microstructure

A partially lithiated SiNWs or SiNPs with a core–shell structure can be decomposed into three numerical domains: two bulk domains, one behind the reaction front (where $c \geq c_+$) and the other in front of the reaction front (where $c < c_-$), and a diffuse interfacial domain (where $c_- < c < c_+$) between the two bulk domains (Yang et al., 2012). Note that $c$ is the Li concentration normalized by that of the fully lithiated phase of $Li_{3.75}Si$, with $c=1$ representing $Li_{3.75}Si$ and $c=0$ pure Si. Here, $c_+$ is assigned to be close to 1, while $c_-$ close to 0. It should be stressed that Li transport in the interfacial domain occurs through chemical reactions that are characterized by the dissociation of the Si–Si bonds and formation of the amorphous $Li_{3.75}Si$, which are expected to differ from the atomic processes of Li diffusion in the lithiated shell (Liu et al., 2012b). Despite such a difference between reaction and diffusion, we simulate the two concurrent processes in a unified manner by treating the interfacial reaction as non-linear diffusion across a diffuse interfacial domain for numerical convenience. One should, however, bear in mind the difference in the physical processes of interfacial reaction and bulk diffusion.

In order to produce a sharp phase boundary with an abrupt change of Li concentration, we set Li diffusivity to be a nonlinear function of Li concentration in the entire system

$$D = D_0\left[\frac{1}{(1-c)} - 2\alpha c\right] \tag{1}$$

where $D_0$ is a diffusion constant and $\alpha$ is a tunable constant that controls the concentration profile near the phase boundary (Liu et al., 2011c; Yang et al., 2012). The singular function yields considerably large Li diffusivity in the lithiated shell ($c=1$), but a finite value ($D_0$) close to the unlithiated core ($c=0$), thereby effectively generating a sharp interface that separates the Li-poor core and the Li-rich shell (Liu et al., 2012b, 2011c). In order to avoid numerical singularity, we set $D=10^5 D_0$ when the value of the singular term in Eq. (1) exceeds $10^5$. It should be pointed out that while the strong nonlinearity of Li diffusivity is essential to produce the sharp interface, the choice of the specific functional form in Eq. (1) is only a matter of computational convenience (Huang et al., 2013).

We next discuss the implementation of orientation-dependent reaction rate at the reaction front during lithiation of $c$-Si. Within the lithiated domains ($c \geq c_+$), the diffusivity is set to be isotropic. Within the interfacial domain ($c_- < c < c_+$), the reaction rate depends on the local crystallographic orientation of the exposed $c$-Si facets. As mentioned previously, the orientation-dependent reaction rate (or interfacial mobility) is modeled by the anisotropic interfacial diffusion across an interfacial domain between the lithiated and unlithiated regions. Based on the experimental data, the orientation-dependent interfacial diffusion constants are set to be $D^F_{0,\langle 110\rangle} = 6D^F_{0,\langle 100\rangle} = 60D^F_{0,\langle 111\rangle}$ (Yang et al., 2012), where the associated orientations are indicated in the subscripts and the superscript "$F$" indicates the constant within the interfacial domain. Here the orientation-dependent interfacial diffusivities play the same role of orientation-dependent reaction rate constants when the interfacial layer is regarded approximately as a sharp interface, as discussed above. A smooth interpolation using the trigonometric functions from the above diffusion constants gives those of other directions (shown in Fig. 3), which are currently unavailable due to the limited experimental data.

The diffusion constant in the lithiated domain, denoted by $D^B_0$, is set to be the same as $D^F_{0,\langle 100\rangle}$, where the superscript "$B$" indicates the bulk domains behind the reaction front. With this setting, the diffusivity $D$ computed by Eq. (1) is significantly

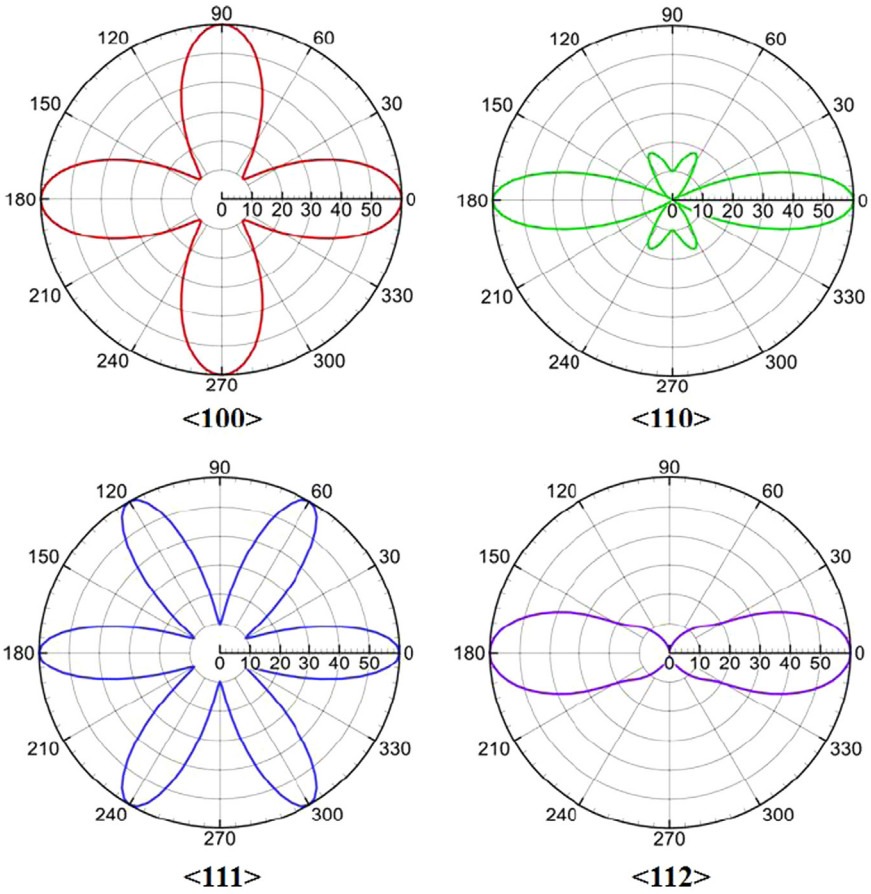


**Fig. 3.** Orientation-dependent diffusion constant (modeling the lithiation reaction rate) at the sharp amorphous–crystalline interface (ACI) on the cross sections of SiNWs with different axial directions.

larger in the lithiated domain than that in the interfacial domain due to the difference in the Li concentrations of these domains. This effectively realizes the two-phase microstructure with a sharp phase boundary whose migration is rate-limiting.

### 3.2. Lithiation induced elasto-plastic deformation

Lithiation of SiNWs or SiNPs results in a core–shell structure. The deformation in the crystalline core simply involves the elastic straining of the lattice. At the sharp reaction front, an abrupt change of Li concentration causes large chemical strains. In addition, the lithiated shell behind the reaction front further undergoes structural relaxation through elasto-plastic deformation (Sethuraman et al., 2010a), which is induced by the pushing-out effect associated with lithiation expansion at the moving, curved reaction front. Considering the lithiation-induced large deformations, the finite-strain plasticity theory is employed to characterize the deformation kinematics and the constitutive relations.

In the finite-strain plasticity framework, deformation is characterized by the elastic and plastic stretch rates (denoted by $\mathbf{d}^e$ and $\mathbf{d}^p$, respectively) and spin rates (denoted by $\mathbf{W}^e$ and $\mathbf{W}^p$, respectively). The total stretch rate tensor $\mathbf{d}$ can be decomposed into three additive parts

$$\mathbf{d}=\mathbf{d}^c+\mathbf{d}^e+\mathbf{d}^p \tag{2}$$

where $\mathbf{d}^c$, $\mathbf{d}^e$, and $\mathbf{d}^p$ are the chemical, elastic, and plastic stretch rates, respectively (Bower, 2010; Bower and Guduru, 2012; Gao and Zhou, 2012, 2013; Zhao et al., 2011b). We assume that the lithiation-induced electrochemical deformation rate is dilational without spin and the electrochemical stretch rate $\mathbf{d}^c$ is proportional to the increment of the Li concentration

$$\mathbf{d}^c=\beta\mathbf{I}\dot{c} \tag{3}$$

where $\beta$ is the lithiation expansion coefficient and $\mathbf{I}$ is the identity tensor. One notices that the chemical strain is analogous to the thermal strain in formulation by considering $\beta$ as the coefficient of thermal expansion and $c$ the temperature. We also assume the isotropic hardening of the lithiated product and accordingly $\mathbf{W}^p=\mathbf{0}$.

We model the unlithiated crystalline core as an isotropic, elastic material, whose stress and strain rates obey classical Hooke's law with two material constants, Young's modulus $Y$ and Poisson's ratio $\nu$. For the lithiated phase, the isotropic elastic and perfectly plastic model is adopted to describe its constitutive response, which relates the stretch and stress rates by the following form:

$$\boldsymbol{\tau}^{\nabla e}=\frac{\hat{Y}}{1+\hat{\nu}}\left[\mathbf{d}^e+\frac{\hat{\nu}}{1-2\hat{\nu}}\mathrm{tr}(\mathbf{d}^e)\mathbf{I}\right] \tag{4}$$

where "tr" denotes the trace of a tensor, $\boldsymbol{\tau}$ is the Kirchhoff stress. The superscripts in $\boldsymbol{\tau}^{\nabla e}$ denote the Jaumann rate of $\boldsymbol{\tau}$, for which the elastic spin is involved. Note that the Kirchhoff stress is related to the Cauchy stress $\boldsymbol{\sigma}$ by $\boldsymbol{\tau}=J\boldsymbol{\sigma}$, where $J$ characterizes the elastic volume expansion (Bower, 2010). Different from the crystalline core for which the elastic constants are fixed values, the two elastic constants, Young's modulus $\hat{Y}$ and Poisson's ratio $\hat{\nu}$, for the lithiated product are phase-dependent, i.e., vary with the Li concentration.

The plastic stretch rate, $\mathbf{d}^p$, obeys the associated $J_2$-flow rule. Namely, plastic yielding occurs when the equivalent stress, $\tau_{eq}=\sqrt{3\mathbf{s}:\mathbf{s}/2}$, reaches the yield strength, $\tau_Y$. Here $\mathbf{s}=\boldsymbol{\tau}-\mathrm{tr}(\boldsymbol{\tau})\mathbf{I}/3$ is the deviatoric stress tensor. In the $J_2$-flow theory, the plastic stretch rate is given by

$$\mathbf{d}^p=\frac{3\mathbf{s}}{2\tau_{eq}}d^p_{eq} \tag{5}$$

where $d^p_{eq}=\sqrt{2\mathbf{d}^p:\mathbf{d}^p/3}$ is the equivalent plastic stretch rate.

The lithiated phase is modeled as an isotropic elastic and perfectly plastic material. However, perfect plasticity often leads to numerical instability in simulations. To circumvent this difficulty, we use the Cowper–Symonds overstress power law with appropriately chosen parameters to approximate the perfectly plastic limit, as

$$d^p_{eq}=m\left(\frac{\tau_{eq}}{\tau_Y}-1\right)^n \tag{6}$$

where $m$ and $n$ are the reference stretch rate and the rate sensitivity exponent, respectively (ABAQUS, 2010).

### 3.3. Boundary value problem

The dynamic evolution of Li concentration, morphological change, and stress generation in lithiated Si can be simulated by solving a coupled boundary value problem. At any given time in a lithiation process, all the material points satisfy the following equilibrium equation:

$$\nabla\cdot\boldsymbol{\sigma}=0 \quad \text{in } V \tag{7}$$

with a traction-free boundary condition

$$\mathbf{n}\cdot\boldsymbol{\sigma}=0 \quad \text{on } S \tag{8}$$

where $\nabla$ represents the vector differential operator with respect to spatial coordinates, $\mathbf{n}$ is the outward normal of the outer surface of the SiNW exposing to Li, $V$ is the volume of the SiNW, and $S$ is the outer surface of the SiNW.

We adopt the classical diffusion equation to describe Li transport in the entire domain

$$\frac{\partial c}{\partial t} = \nabla \cdot (D \nabla c) \quad \text{in } V \tag{9}$$

The Dirichlet boundary condition is imposed on the circumference $\Gamma$ of the circular cross section at one end of the SiNW

$$c = 1 \quad \text{on } \Gamma. \tag{10}$$

## 4. Numerical implementation

### 4.1. Model parameters

To simulate the dynamic evolution of the core–shell structure in lithiated SiNWs, the coupled chemo-mechanical model is implemented in the finite element package ABAQUS (ABAQUS, 2010). As diffusion and heat conduction are dictated by the same type of governing equation (Eq. (9)), we simulate Li diffusion by solving a surrogate heat conduction problem, where the normalized Li concentration $c$ is regarded as temperature $T$ in heat conduction (Huang et al., 2013; Liu et al., 2011c; Pharr et al., 2012; Yang et al., 2012; Zhao et al., 2012). Accordingly, the lithiation-induced electrochemical stretch rate $\mathbf{d}^c$ is simulated by a thermal strain rate and the lithiation expansion coefficient $\beta$ is then equivalently treated as the coefficient of thermal expansion. Using the implicit coupled temperature–displacement procedure in ABAQUS/Standard, the corresponding Li concentration and stress–strain fields are updated incrementally. Meanwhile, the user subroutine UMATHT interfaces with ABAQUS to dynamically update the diffusivities based on the instantaneous Li distribution profile.

Using the coupled chemo-mechanical model, the morphological evolutions and stress generation of the four three-dimensional SiNWs with different axial orientations (⟨100⟩, ⟨110⟩, ⟨111⟩, and ⟨112⟩ in Fig. 1) are simulated (Lee et al., 2011; Liu et al., 2011c). Prior to lithiation, the cross sections of all the SiNWs are circular with a radius of $R$. Due to symmetry of the cross section, only a quarter of each SiNW is simulated with appropriately imposed symmetrical boundary conditions in order to reduce the computational cost.

All the material parameters are specified according to experimental data whenever possible. The yield stress $\tau_Y$ for the fully lithiated phase, $Li_{3.75}Si$, is set to be 1.5 GPa (Chon et al., 2011; Sethuraman et al., 2010a, 2010b). The simulation domain is carefully meshed to ensure numerical stability and convergence. The material parameters $m$ and $n$ in Eq. (7) are set to be $m = 1000(1/s)$ and $n = 1$, respectively, which yield a nearly rate-independent behavior. Young's modulus $\hat{Y}$ and Poisson's ratio $\hat{\nu}$ of the lithiated product are both assumed to linearly vary with Li concentration, i.e., from 160 to 40 GPa and from 0.24 to 0.22 (Fan et al., 2013; Shenoy et al., 2010; Wortman and Evans, 1965; Zhao et al., 2011a), respectively, as $c$ varies from 0 ($c$-Si, $\hat{Y} = Y$ and $\hat{\nu} = \nu$) to 1 (the fully lithiated phase). The chemical dilational coefficient is chosen to be $\beta = 0.6$ in order to match the 300% volume expansion in the fully lithiated phase.

### 4.2. Treatment of interfacial domain

The model involves a careful treatment of the interfacial domain. At any instant, the narrow interfacial domain ($c_- < c < c_+$) is identified based on the Li concentration profile. We chose $c_- = 0.02$ and $c_+ = 0.98$. At any point within such an interfacial domain, the local interfacial orientation is determined from the direction of the largest Li concentration gradient, i.e. that of the resultant concentration gradient vector. Based on the component of the concentration gradient vector in the cross-sectional plane, the diffusion constants $D_0$ along these directions can be calculated from the interpolated function of the orientation-dependent diffusion constant, as shown in Fig. 3. However, Li diffusivity on the surface of SiNWs, irrespective of the local interfacial orientation, is set to be two orders of magnitude larger than that in the bulk, which reflects the much faster Li diffusion on the surface of SiNWs than in the bulk. The Li concentration profile is then updated to simulate the migration of the phase boundary in the SiNWs.

As will be demonstrated later, the interfacial domain identified spans only a few elements in finite element simulations, demonstrating its sharpness. In addition, the thickness of the interfacial domain remains roughly the same throughout the simulation. One notes that the experimentally observed thickness of the amorphous-crystalline interface is about $\delta \sim 1$ nm (Chon et al., 2011). The simulated interfacial domain thus conveniently defines a characteristic length scale in the finite element model that would be otherwise scale independent.

## 5. Numerical results

### 5.1. Lithiation induced anisotropic swelling: small strain model

We next use a 3D finite element, small-strain model to simulate the morphological change and stress generation in SiNWs. Fig. 4 shows the morphologies of four lithiated SiNWs with their crystallographic orientations shown in Fig. 1. The dynamic Li transport in the axial and radial directions of the SiNWs are indicated by the color contours, with

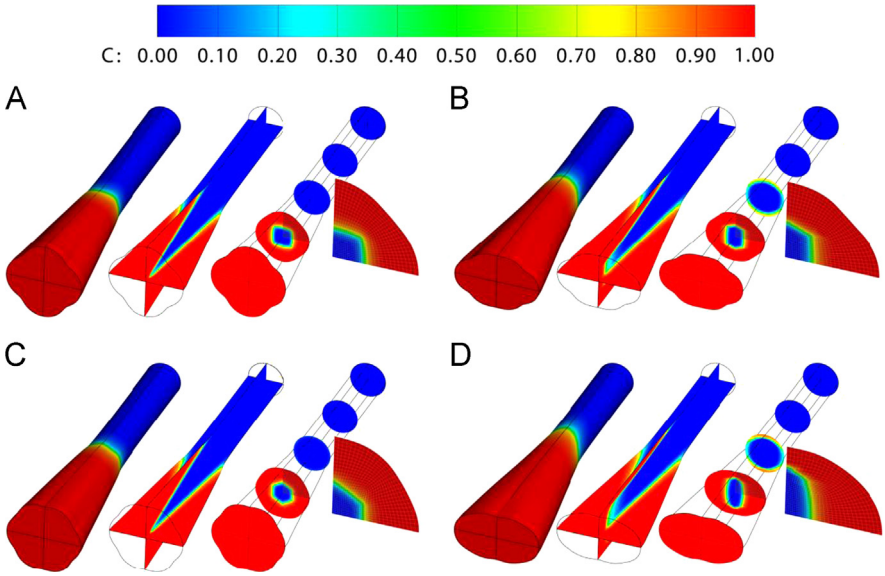


**Fig. 4.** 3D morphologies of the lithiated SiNWs of different axial crystallographic orientations: (A) ⟨100⟩, (B) ⟨110⟩, (C) ⟨111⟩, and (D) ⟨112⟩. The Li concentrations on the surface and different cross sections are indicated by the contours. Transition colors from red to blue indicate the reaction fronts. In each SiNW, a quarter of the partially lithiated cross section (shaded) is highlighted by an enlarged image with finite element meshes attached, showing that the width of the simulated interface is only a few elements. (For interpretation of the references to color in this figure legend, the reader is referred to the web version of this article.)

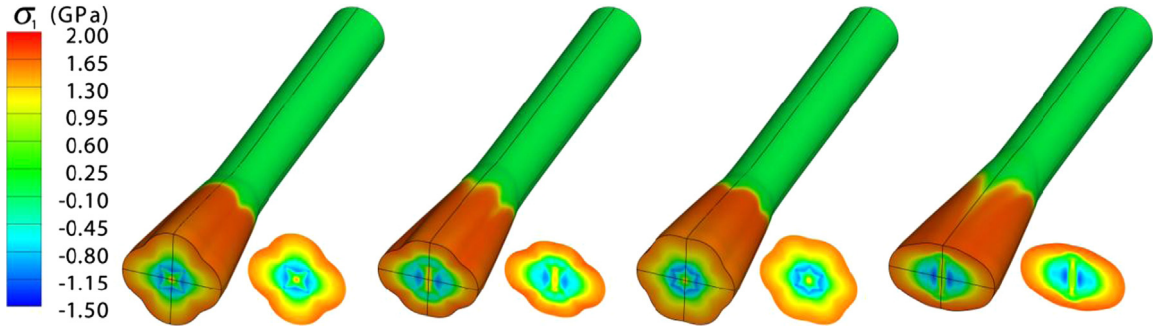


**Fig. 5.** Stress distributions (based on small-strain theory) in the lithiated SiNWs (from left to right: ⟨100⟩, ⟨110⟩, ⟨111⟩, and ⟨112⟩) at the lithiation snapshots $t=0.3$, where $t$ is the normalized time.

red representing the nearly fully lithiated amorphous Si phase ($Li_{3.75}Si$) and blue the crystalline Si phase. For each SiNW, three subfigures respectively display the overall deformation morphology, the Li concentration profiles along the radial direction and along the axial direction. In each subfigure, a quarter of partially lithiated cross section (shaded) is displayed by an enlarged image with finite element meshes attached, showing the width of the interface is only a few elements.

As the Li diffusivity on the surface of SiNWs is much larger than that in the bulk, the surface of the SiNWs acts as a fast Li transport path. It follows that the cross sections along the axial direction are lithiated in a similar fashion: Li flows radially inward, forming a two-phase core–shell structure separated by a sharp interface. As shown in Fig. 4, the cross sections close to the end are fully lithiated. Within the partially lithiated cross sections, the reaction fronts form polygonal shapes. The unlithiated core tapers along the axial direction of SiNWs. The development of the faceted reaction front is due to the much higher mobility of {110} phase boundaries than others. From the fully lithiated end to the remote unlithiated end of the nanowire, the remaining core of unlithiated *c*-Si becomes progressively larger. Thus, the core–shell structures of different cross sections along the axial direction at any instant can be effectively considered as the dynamic lithiation process of a single representative cross section. It should be noted that as lithiation proceeds, only the {110} facets survive eventually at the core–shell interface. The simulated two-phase microstructure and morphological evolution of the SiNWs agree closely with the experimental observations (Lee et al., 2011; Liu et al., 2011c), as shown in Fig. 1.

Fig. 5 shows the maximal principal Cauchy stress (denoted by $\sigma_1$) in the four SiNWs at the lithiation snapshot $t=0.3$, where $t$ is normalized by the total time required to fully lithiate the front end of the SiNWs. We note that the small-strain model captures the general trend of stress distribution in the lithiated SiNWs, i.e., the development of hoop tension in the lithiated outer shell and compression near the reaction front. However, the simulated stress distribution does not exhibit

significant concentration of hoop tension in the surface layer, implying that fracture may initiate at any circumferential position at the outer surface, which contradicts with the well-defined fracture sites observed in previous experiments (Lee et al., 2012; Liang et al., 2013; Liu et al., 2011c). Such discrepancy arises from the small-strain theory used in our 3D simulations, to be shown in the next section.

### 5.2. Lithiation-induced anisotropic fracture: finite-strain model

We next simulate the 3D morphological change and stress evolution of the SiNWs based on the finite-strain model, but with the same boundary conditions as adopted in the small-strain model. Fig. 6 plots the maximal principal Cauchy stress (denoted by $\sigma_1$) at the lithiation snapshots $t=0.3$, where $t$ is again normalized by the total time required to fully lithiate the front end of the four SiNWs. The predicted morphological changes of the cross sections for all the SiNWs due to lithiation are similar to those by the small-strain model. Importantly, the finite-strain analysis predicts concentration of hoop tension at particular angular sites of the cross sections in the SiNWs, indicating the onset fracture locations. The predicted sites of onset fracture agree with the recent experimental studies (Lee et al., 2012; Liang et al., 2013; Liu et al., 2011c), as shown in Fig. 1.

As our model involves large plastic deformation and dynamically couples Li diffusion and mechanics, the 3D model is computationally expansive, particularly when relatively fine meshes are used. Since different cross sections in each of the

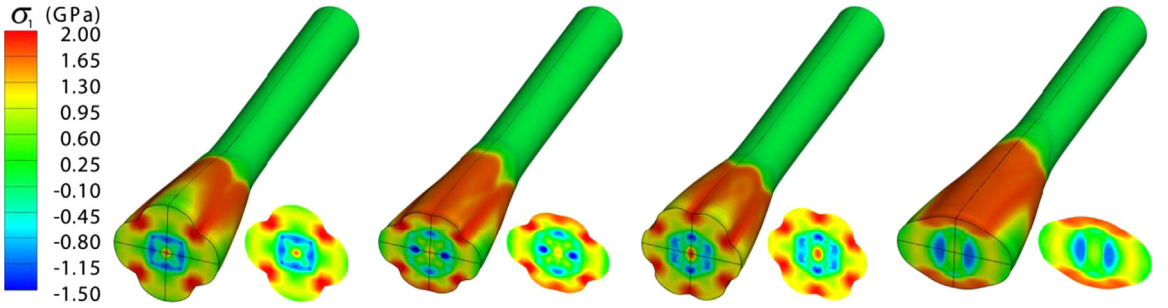


**Fig. 6.** Stress distributions (based on finite-strain theory) in the lithiated SiNWs (from left to right: ⟨100⟩, ⟨110⟩, ⟨111⟩, and ⟨112⟩) at the lithiation snapshots $t=0.3$, where $t$ is the normalized time.

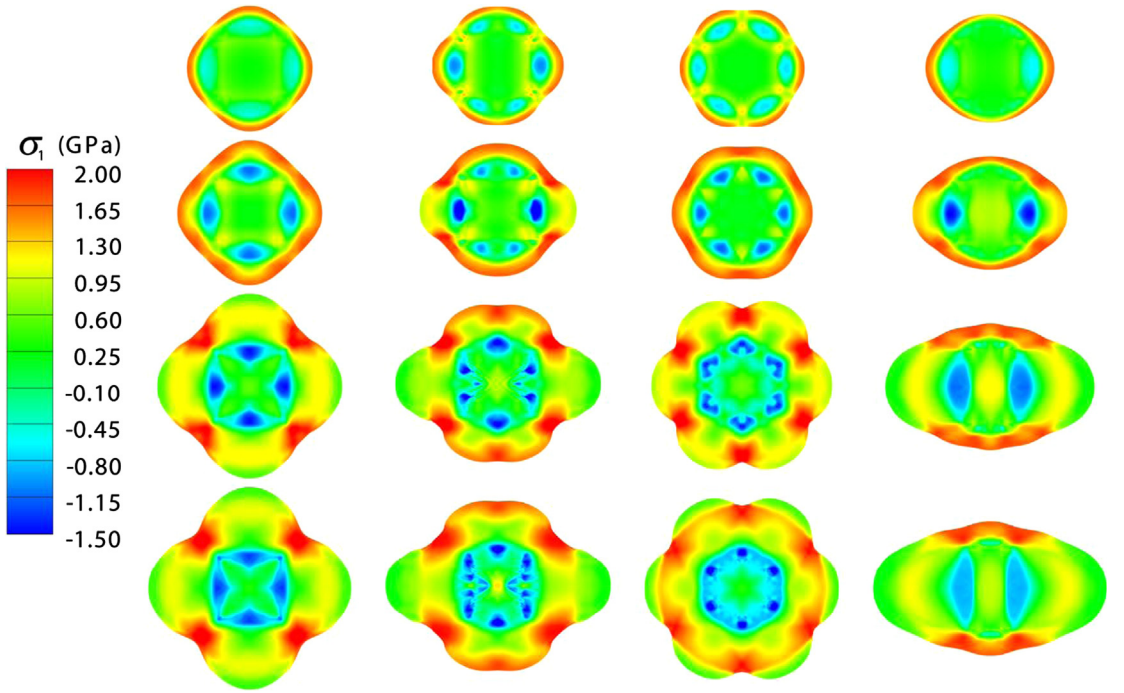


**Fig. 7.** Stress contours (the maximal principal stress) in the lithiated SiNWs. From left to right, the four columns represent the morphological changes and stress distribution in ⟨100⟩, ⟨110⟩, ⟨111⟩, and ⟨112⟩ SiNWs, respectively. Each column includes four simulation snapshots ($t=0.015$, 0.05, 0.2 and 0.3, where $t$ is the normalized time) of the SiNWs being lithiated.

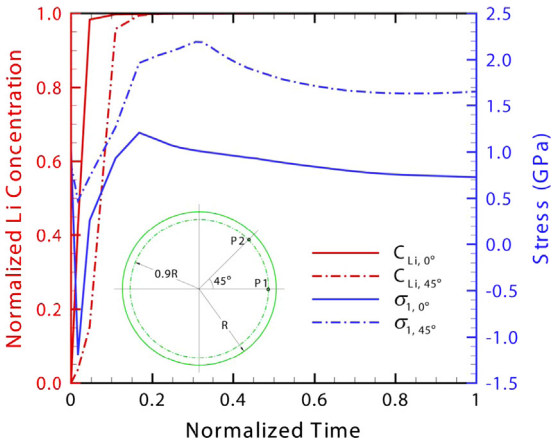


**Fig. 8.** Evolution of Li concentration and the principal stresses of two representative material points in the ⟨100⟩ SiNW. Both points are located at $r=0.9R$ in the pristine state of the SiNW, where $R$ is the radius of the SiNW. Point 1 (P1) is located along the largest expansion direction (⟨110⟩ direction, $\theta=0^\circ$), and Point 2 (P2) along the least expansion direction (⟨100⟩ direction, $\theta=45^\circ$).

SiNWs are lithiated in a similar manner, a two-dimensional (2D) model may be well suited to capture the stress generation in the SiNWs. In accordance to the negligible expansion along the axial direction of the SiNWs observed in experiments (Lee et al., 2011), the plain-strain condition can be justified and imposed in the 2D simulations. We set $c=1$ at the outer boundary of the cross section. Fig. 7 plots the maximal principal Cauchy stress ($\sigma_1$) at four different lithiation snapshots $t=0.015$, 0.05, 0.2 and 0.3, where $t$ is normalized by the total time required to fully lithiate each of the cross sections. One notes that the stress distribution profiles on the cross sections in the SiNWs obtained by the 2D simulations agree closely to those by the 3D model, demonstrating the validity of the 2D model.

We next rationalize the origin of the anisotropic fracture, i.e., onset fracture occurs at particular angular sites of the cross sections in the SiNWs. It should be noted that the maximal principal stress $\sigma_1$ represents the hoop component at the symmetric planes, and closely approximates the hoop component anywhere else. As seen from the stress contours, the hoop component $\sigma_1$ is tensile in the outer surfaces, while compressive near the reaction fronts. The hoop tension near the outer surface stems from the "pushing-out" effect, i.e., the large volume expansion at the reaction front causes the radial expansion and accordingly hoop stretch in the materials behind the reaction front. We also observed that the concentrated stress develops at the early stage of lithiation. The levels of stress concentration ($\sim 1.5\tau_Y$) are almost the same for the four SiNWs. Interestingly, the stress concentration exclusively occurs at the angular sites between two adjacent {110} facets for all the four SiNWs. The development of such stress concentrations at the specific angular sites near the outer surface can be attributed to the pushing-out effect of the newly lithiated product from the two adjacent {110} facets at the reaction front. As the pushing-out effect generates large expansion normal to the {110} facets, the materials located at the intersection of the two adjacent {110} facets undergo large and non-uniform stretch, leading to stress concentration. The concentrated stress may well exceed the fracture strength of the amorphous lithiated Si. As a result, fracture initiates at the specified angular sites near the outer surfaces of the lithiated SiNWs.

Fig. 8 plots the evolution of the maximal principal stress experienced by two representative material points along with that of the Li concentration at the points in the ⟨100⟩ SiNW of the 2D models. The two material points are located at $r=0.9R$ along the maximal ($\theta=0^\circ$, denoted by point 1) and minimal ($\theta=45^\circ$, a stress concentration site, denoted by point 2) radial expansion directions, respectively, of the ⟨100⟩ SiNW in the pristine state, as marked in the inset of Fig. 8. As the material points are very close to the outer surface of the SiNW, the reaction front reaches the material points in a very short time at which the Li concentration begins to rise, and rapidly reaches to unity, i.e., the fully lithiated state. Point 1 is lithiated earlier than Point 2 since the former is right along the primary Li flow direction, i.e., the ⟨110⟩ direction. As the reaction front sweeps through the material points, the principal stress decreases, reaches a minimum, and then rapidly increases to its maximum. For Point 1, the principal stress even changes its sign twice (from tension, compression, to tension) when the reaction front sweeps through it. As lithiation continues, the principal stresses at these two points vary insignificantly. It should be noted that Point 2 experiences a maximal stress double more than that at Point 1, clearly indicating that it is the onset site of fracture.

## 6. Discussions

The present modeling framework can be extended in several aspects, particularly regarding the stress-mediated lithiation rate and size-dependent fracture. In general, Li insertion generates hydrostatic compression both at and closely behind the reaction front in solid-state electrodes. The compressive stress may suppress Li reaction at the reaction front as well as Li diffusion behind it, thus slowing down further lithiation. Such stress retardation of lithiation has been

demonstrated by recent *in-situ* TEM studies: the migration of the lithiation reaction front in both SiNWs and SiNPs slowed down considerably as lithiation proceeded (Liu et al., 2012a; McDowell et al., 2012). The lithiation-induced hydrostatic compression in Si could be high enough to completely override the electrochemical driving forces on reaction and diffusion, leading to the stagnation of lithiation.

Lithiation retardation can be characterized by incorporating the stress effects on the lithiation kinetics. Both the reaction rate at the reaction front and the diffusion rate in the lithiated region may be set to be stress dependent, e.g.,

$$D_{eff} = D \exp(-p\Omega/k_B T) \tag{11}$$

where $D$ is the Li diffusivity in the stress-free condition, defined in Eq. (1), $\Omega$ is the activation volume of Li diffusion, $k_B T$ is the thermal energy, and $p$ is the pressure that can be obtained from the trace of the symmetric Cauchy stress tensor $\boldsymbol{\sigma}$ (Cui et al., 2013; Haftbaradaran et al., 2010; Liu et al., 2012a). It should be pointed out that stress gradient can also regulate the lithiation kinetics in solid electrodes (Grantab and Shenoy, 2012; Yang et al., 2013). The effect of stress gradient can be incorporated into the model by relating the stress gradient to the Li flux, as shown recently (Grantab and Shenoy, 2012). These studies clearly showed the strong coupling between lithiation-generated stress and lithiation kinetics. In a recent effort, we demonstrated that externally applied forces can be exploited to regulate lithiation rate and rate anisotropy (Gu et al., 2014). Given the intimate relations between lithiation rate anisotropy and the fracture of *c*-Si electrodes, this study opens a possible pathway to mitigate the degradation of *c*-Si during electrochemical cycling.

Within the framework of finite-strain plasticity, the present model accurately predicts the locations of stress concentration, consistent with the experimentally observed crack nucleation sites in lithiated SiNWs. Once nucleated, subsequent crack propagation is size dependent, as shown in our recent experiments (Liu et al., 2012d). Such size dependence of fracture can be understood in terms of flaw tolerance in small systems. For a SiNW with a sufficiently small diameter, the energy release rate during crack extension is dominantly governed by the sample size (i.e., the diameter of cross section) rather than the flaw size, i.e., an increase of the sample size can raise the energy release rate of crack extension, given the same size of the crack. When the SiNW exceeds a critical diameter, the energy release rate becomes large enough to drive crack growth. In addition, we note that the coupling between lithiation chemistry and crack mechanics involves the interplay between the crack-tip stress field and the local Li reaction–diffusion (Grantab and Shenoy, 2012; Yang et al., 2013). A detailed study of crack extension in lithiated Si that incorporates these factors is currently underway.

## 7. Concluding remarks

In conclusion, we have formulated a finite-strain chemo-mechanical model to study the lithiation-induced phase change, large deformation and fracture in *c*-Si in a 3D setting. The modeling framework incorporates several key features observed from HRTEM studies, including the sharp amorphous-crystalline interface, anisotropic interface mobility and large deformation. The model also couples the Li reaction–diffusion with deformation mechanics in unidirectional manner, i.e., lithiation induces strain and stress. By considering the effect of lithiation-induced stress on Li reaction–diffusion kinetics, the model can be further extended to bidirectional coupling. Though only *c*-SiNWs were simulated in this study, the modeling platform can be extended to *a*-Si (by turning off the anisotropic mobility of the reaction front) and other high-capacity electrode materials (with experimentally verified materials properties).

Using the chemo-mechanical model, we simulated the morphological evolution and stress generation in SiNWs upon lithiation. Our simulation results show that the anisotropic interfacial Li mobility significantly impacts the morphological changes and stress concentration in lithiated Si. Owing to the much faster reaction rate along the ⟨110⟩ directions, the unlithiated cores exhibit polygonal shapes with {110} facets. The large deformation occurring at the reaction front, i.e., {110} facets, pushes the lithiated product outward, resulting in large anisotropic swelling as well as stress concentrations at the angular sites between adjacent {110} facets in the lithiated shell. In addition, Li insertion can induce high hydrostatic pressure at and closely behind the reaction front, as shown in our simulation results, which may explain the lithiation retardation observed by *in-situ* TEM studies. We found that the 3D small-strain model can capture the morphological changes and the general trend of stress distribution during lithiation. In contrast, the 3D finite-strain model captures not only the morphological evolution, but also the concentration of hoop tension, and thus predicting the onset fracture sites in the lithiated SiNWs. Since all the cross sections in the SiNWs are lithiated in a similar manner with insignificant elongation along the axial directions, we demonstrated that a 2D finite-strain model with the plane-strain condition is well suited to accurately resolve the stress concentration during the lithiation process. Such a 2D model is advantageous for its significantly reduced computational cost. Both the morphological changes and fracture sites predicted by our finite-strain models agree well with the previous experimental studies. In addition to presenting a chemo-mechanical model for the study of lithiation-induced degradation in high-capacity electrode materials, the mechanistic understanding of micro-structural evolution and stress generation in our study shed lights onto the design of next-generation failure-resistant electrodes.

## Acknowledgements

SLZ acknowledges support by the NSF grant CMMI-0900692. TZ acknowledges support by the NSF grant CMMI-1100205. XG acknowledges the support from China National Natural Science Foundation (Grant nos. 10925209, 91216201) and Program for Changjiang Scholars.

## References

ABAQUS, 2010. Abaqus Analysis User's Manual. Dassault Systemes, Providence, RI, USA Version 6.10.
Arico, A.S., Bruce, P., Scrosati, B., Tarascon, J.-M., van Schalkwijk, W., 2005. Nanostructured materials for advanced energy conversion and storage devices. Nat. Mater. 4, 366–377.
Beaulieu, L.Y., Eberman, K.W., Turner, R.L., Krause, L.J., Dahn, J.R., 2001. Colossal reversible volume changes in lithium alloys. Electrochem. Solid State Lett. 4, A137–A140.
Bindumadhavan, K., Srivastava, S.K., Mahanty, S., 2013. MoS2-MWCNT hybrids as a superior anode in lithium-ion batteries. Chem. Commun. 49, 1823–1825.
Bower, A.F., 2011. Applied Mechanics of Solids. CRC Press, Boca Raton, FL.
Bower, A.F., Guduru, P.R., 2012. A simple finite element model of diffusion, finite deformation, plasticity and fracture in lithium ion insertion electrode materials. Model. Simul. Mater. Sci. Eng. 20, 045004.
Bruce, P.G., Scrosati, B., Tarascon, J.M., 2008. Nanomaterials for rechargeable lithium batteries. Angew. Chem. Int. Ed. 47, 2930–2946.
Chan, C.K., Peng, H.L., Liu, G., McIlwrath, K., Zhang, X.F., Huggins, R.A., Cui, Y., 2008. High-performance lithium battery anodes using silicon nanowires. Nat. Nanotechnol. 3, 31–35.
Chon, M.J., Sethuraman, V.A., McCormick, A., Srinivasan, V., Guduru, P.R., 2011. Real-time measurement of stress and damage evolution during initial lithiation of crystalline silicon. Phys. Rev. Lett. 107, 045503.
Cui, L.F., Ruffo, R., Chan, C.K., Peng, H.L., Cui, Y., 2009. Crystalline-amorphous core–shell silicon nanowires for high capacity and high current battery electrodes. Nano Lett. 9, 491–495.
Cui, Z., Gao, F., Qu, J., 2013. Interface-reaction controlled diffusion in binary solids with applications to lithiation of silicon in lithium-ion batteries. J. Mech. Phys. Solids 61, 293–310.
Fan, F., Huang, S., Yang, H., Raju, M., Datta, D., Shenoy, V.B., vanDuin, A.C.T., Zhang, S., Zhu, T., 2013. Mechanical properties of amorphous $Li_xSi$ alloys: a reactive force field study. Model. Simul. Mater. Sci. Eng. 21, 074002.
Gao, Y.F., Zhou, M., 2012. Strong dependency of lithium diffusion on mechanical constraints in high-capacity Li-ion battery electrodes. Acta Mech. Sin. 28, 1068–1077.
Gao, Y.F., Zhou, M., 2013. Coupled mechano-diffusional driving forces for fracture in electrode materials. J. Power Sources 230, 176–193.
Goldman, J.L., Long, B.R., Gewirth, A.A., Nuzzo, R.G., 2011. Strain Anisotropies and self-limiting capacities in single-crystalline 3D silicon microstructures: models for high energy density lithium-ion battery anodes. Adv. Funct. Mater. 21, 2412–2422.
Grantab, R., Shenoy, V.B., 2012. Pressure-gradient dependent diffusion and crack propagation in lithiated silicon nanowires. J. Electrochem. Soc. 159, A584–A591.
Gu, M., Yang, H., Perea, D.E., Zhang, J.-G., Zhang, S., Wang, C.-M., 2014. Bending-induced symmetry breaking of lithiation in germanium nanowires. Nano Lett., http://dx.doi.org/10.1021/nl501680w.
Haftbaradaran, H., Gao, H., Curtin, W.A., 2010. A surface locking instability for atomic intercalation into a solid electrode. Appl. Phys. Lett. 96, 091909. (091903).
Hertzberg, B., Alexeev, A., Yushin, G., 2010. Deformations in Si–Li anodes upon electrochemical alloying in nano-confined space. J. Am. Chem. Soc. 132, 8548–8549.
Huang, S., Fan, F., Li, J., Zhang, S., Zhu, T., 2013. Stress generation during lithiation of high-capacity electrode particles in lithium ion batteries. Acta Mater. 61, 4354–4364.
Lee, S.W., McDowell, M.T., Berla, L.A., Nix, W.D., Cui, Y., 2012. Fracture of crystalline silicon nanopillars during electrochemical lithium insertion. Proc. Natl. Acad. Sci. USA 109, 4080–4085.
Lee, S.W., McDowell, M.T., Choi, J.W., Cui, Y., 2011. Anomalous shape changes of silicon nanopillars by electrochemical lithiation. Nano Lett. 11, 3034–3039.
Li, H., Huang, X.J., Chen, L.Q., Wu, Z.G., Liang, Y., 1999. A high capacity nano-Si composite anode material for lithium rechargeable batteries. Electrochem. Solid State Lett. 2, 547–549.
Liang, W., Yang, H., Fan, F., Liu, Y., Liu, X.H., Huang, J.Y., Zhu, T., Zhang, S., 2013. Tough germanium nanoparticles under electrochemical cycling. ACS Nano 7, 3427–3433.
Liu, X.H., Fan, F., Yang, H., Zhang, S., Huang, J.Y., Zhu, T., 2012a. Self-limiting lithiation in silicon nanowires. ACS Nano 7, 1495–1503.
Liu, X.H., Huang, J.Y., 2011. In situ TEM electrochemistry of anode materials in lithium ion batteries. Energy Environ. Sci. 4, 3844–3860.
Liu, X.H., Huang, S., Picraux, S.T., Li, J., Zhu, T., Huang, J.Y., 2011a. Reversible nanopore formation in ge nanowires during lithiation–delithiation cycling: an in situ transmission electron microscopy study. Nano Lett. 11, 3991–3997.
Liu, X.H., Wang, J.W., Huang, S., Fan, F., Huang, X., Liu, Y., Krylyuk, S., Yoo, J., Dayeh, S.A., Davydov, A.V., Mao, S.X., Picraux, S.T., Zhang, S., Li, J., Zhu, T., Huang, J.Y., 2012b. In situ atomic-scale imaging of electrochemical lithiation in silicon. Nat. Nanotechnol. 7, 749–756.
Liu, X.H., Wang, J.W., Liu, Y., Zheng, H., Kushima, A., Huang, S., Zhu, T., Mao, S.X., Li, J., Zhang, S., Lu, W., Tour, J.M., Huang, J.Y., 2012c. In situ transmission electron microscopy of electrochemical lithiation, delithiation and deformation of individual graphene nanoribbons. Carbon 50, 3836–3844.
Liu, X.H., Zhang, L.Q., Zhong, L., Liu, Y., Zheng, H., Wang, J.W., Cho, J.-H., Dayeh, S.A., Picraux, S.T., Sullivan, J.P., Mao, S.X., Ye, Z.Z., Huang, J.Y., 2011b. Ultrafast electrochemical lithiation of individual Si nanowire anodes. Nano Lett. 11, 2251–2258.
Liu, X.H., Zheng, H., Zhong, L., Huang, S., Karki, K., Zhang, L.Q., Liu, Y., Kushima, A., Liang, W.T., Wang, J.W., Cho, J.-H., Epstein, E., Dayeh, S.A., Picraux, S.T., Zhu, T., Li, J., Sullivan, J.P., Cumings, J., Wang, C., Mao, S.X., Ye, Z.Z., Zhang, S., Huang, J.Y., 2011c. Anisotropic swelling and fracture of silicon nanowires during lithiation. Nano Lett. 11, 3312–3318.
Liu, X.H., Zhong, L., Huang, S., Mao, S.X., Zhu, T., Huang, J.Y., 2012d. Size-dependent fracture of silicon nanoparticles during lithiation. ACS Nano 6, 1522–1531.
Liu, Y., Zheng, H., Liu, X.H., Huang, S., Zhu, T., Wang, J., Kushima, A., Hudak, N.S., Huang, X., Zhang, S., Mao, S.X., Qian, X., Li, J., Huang, J.Y., 2011d. Lithiation-induced embrittlement of multiwalled carbon nanotubes. ACS Nano 5, 7245–7253.
Magasinski, A., Dixon, P., Hertzberg, B., Kvit, A., Ayala, J., Yushin, G., 2010. High-performance lithium-ion anodes using a hierarchical bottom-up approach. Nat. Mater. 9, 353–358.
Marom, R., Amalraj, S.F., Leifer, N., Jacob, D., Aurbach, D., 2011. A review of advanced and practical lithium battery materials. J. Mater. Chem. 21, 9938–9954.
McDowell, M.T., Lee, S.W., Harris, J.T., Korgel, B.A., Wang, C., Nix, W.D., Cui, Y., 2013. In situ tem of two-phase lithiation of amorphous silicon nanospheres. Nano Lett. 13, 758–764.
McDowell, M.T., Ryu, I., Lee, S.W., Wang, C., Nix, W.D., Cui, Y., 2012. Studying the kinetics of crystalline silicon nanoparticle lithiation with in situ transmission electron microscopy. Adv. Mater. 24, 6034–6041.
Newnham, R.E., 2005. Properties of Materials: Anisotropy, Symmetry, Structure. Oxford University Press, New York.

Obrovac, M.N., Christensen, L., 2004. Structural changes in silicon anodes during lithium insertion/extraction. Electrochem. Solid State Lett. 7, A93–A96.
Park, M.H., Kim, M.G., Joo, J., Kim, K., Kim, J., Ahn, S., Cui, Y., Cho, J., 2009. Silicon nanotube battery anodes. Nano Lett. 9, 3844–3847.
Pharr, M., Zhao, K., Wang, X., Suo, Z., Vlassak, J.J., 2012. Kinetics of initial lithiation of crystalline silicon electrodes of lithium-ion batteries. Nano Lett. 12, 5039–5047.
Ryu, I., Choi, J.W., Cui, Y., Nix, W.D., 2011. Size-dependent fracture of Si nanowire battery anodes. J. Mech. Phys. Solids 59, 1717–1730.
Scrosati, B., Hassoun, J., Sun, Y.K., 2011. Lithium-ion batteries. A look into the future. Energy Environ. Sci. 4, 3287–3295.
Service, R.F., 2011. Getting there. Science 332, 1494–1496.
Sethuraman, V.A., Chon, M.J., Shimshak, M., Srinivasan, V., Guduru, P.R., 2010a. In situ measurements of stress evolution in silicon thin films during electrochemical lithiation and delithiation. J. Power Sources 195, 5062–5066.
Sethuraman, V.A., Srinivasan, V., Bower, A.F., Guduru, P.R., 2010b. In situ measurements of stress-potential coupling in lithiated silicon. J. Electrochem. Soc. 157, A1253–A1261.
Shenoy, V.B., Johari, P., Qi, Y., 2010. Elastic softening of amorphous and crystalline Li–Si phases with increasing Li concentration: a first-principles study. J. Power Sources 195, 6825–6830.
Sun, C.-F., Karki, K., Jia, Z., Liao, H., Zhang, Y., Li, T., Qi, Y., Cumings, J., Rubloff, G.W., Wang, Y., 2013. A beaded-string silicon anode. ACS Nano 7, 2717–2724.
Tarascon, J.M., Armand, M., 2001. Issues and challenges facing rechargeable lithium batteries. Nature 414, 359–367.
Wang, J.W., He, Y., Fan, F., Liu, X.H., Xia, S., Liu, Y., Harris, C.T., Li, H., Huang, J.Y., Mao, S.X., Zhu, T., 2013. Two-phase electrochemical lithiation in amorphous silicon. Nano Lett. 13, 709–715.
Wortman, J.J., Evans, R.A., 1965. Young's modulus, shear modulus, and Poisson's ratio in silicon and germanium. J. Appl. Phys. 36, 153–156.
Wu, H., Chan, G., Choi, J.W., Ryu, I., Yao, Y., McDowell, M.T., Lee, S.W., Jackson, A., Yang, Y., Hu, L.B., Cui, Y., 2012. Stable cycling of double-walled silicon nanotube battery anodes through solid-electrolyte interphase control. Nat. Nanotechnol. 7, 309–314.
Yamada, M., Ueda, A., Matsumoto, K., Ohzuku, T., 2011. Silicon-based negative electrode for high-capacity lithium-ion batteries: “SiO”–carbon composite. J. Electrochem. Soc. 158, A417–A421.
Yang, H., Huang, S., Huang, X., Fan, F., Liang, W., Liu, X.H., Chen, L.-Q., Huang, J.Y., Li, J., Zhu, T., Zhang, S., 2012. Orientation-dependent interfacial mobility governs the anisotropic swelling in lithiated silicon nanowires. Nano Lett. 12, 1953–1958.
Yang, H., Huang, X., Liang, W., van Duin, A.C.T., Raju, M., Zhang, S., 2013. Self-weakening in lithiated graphene electrodes. Chem. Phys. Lett. 563, 58–62.
Yao, Y., McDowell, M.T., Ryu, I., Wu, H., Liu, N., Hu, L., Nix, W.D., Cui, Y., 2011. Interconnected silicon hollow nanospheres for lithium-ion battery anodes with long cycle life. Nano Lett. 11, 2949–2954.
Zhang, L.Q., Liu, X.H., Liu, Y., Huang, S., Zhu, T., Gui, L., Mao, S.X., Ye, Z.Z., Wang, C.M., Sullivan, J.P., Huang, J.Y., 2011. Controlling the lithiation-induced strain and charging rate in nanowire electrodes by coating. ACS Nano 5, 4800–4809.
Zhang, Q.F., Zhang, W.X., Wan, W.H., Cui, Y., Wang, E.G., 2010. Lithium insertion in silicon nanowires: an ab initio study. Nano Lett. 10, 3243–3249.
Zhang, W.J., 2011. A review of the electrochemical performance of alloy anodes for lithium-ion batteries. J. Power Sources 196, 13–24.
Zhao, K., Pharr, M., Wan, Q., Wang, W.L., Kaxiras, E., Vlassak, J.J., Suo, Z., 2012. Concurrent reaction and plasticity during initial lithiation of crystalline silicon in lithium-ion batteries. J. Electrochem. Soc. 159, A238–A243.
Zhao, K., Wang, W.L., Gregoire, J., Pharr, M., Suo, Z., Vlassak, J.J., Kaxiras, E., 2011a. Lithium-assisted plastic deformation of silicon electrodes in lithium-ion batteries: a first-principles theoretical study. Nano Lett. 11, 2962–2967.
Zhao, K.J., Pharr, M., Vlassak, J.J., Suo, Z.G., 2011b. Inelastic hosts as electrodes for high-capacity lithium-ion batteries. J. Appl. Phys. 109, 016110.